JOURNAL OF GEOPHYSICAL RESEARCH, VOL. 94, NO. B7, PAGES 9607–9613, JULY 10, 1989

Influence of Focal Mechanism on Peak Accelerations of Strong Motions of the Whittier Narrows, California, Earthquake and an Aftershock

JOHN E. VIDALE

University of California, Santa Cruz

Focal mechanisms affect the pattern of the peak accelerations of the October 1, 1987 Whittier Narrows earthquake and its October 4 aftershock. The peak accelerations observed on 21 Strong Motion Instrumentation Program and 22 U.S. Geological Survey accelerograms correlate well with the ratio of shear wave amplitude computed from the thrust mechanism of the main shock and the strike-slip mechanism of the aftershock. This correlation means that seismic energy is radiated from the fault with close to the standard double-couple radiation pattern at the frequencies 3–6 Hz corresponding to the peak accelerations.

INTRODUCTION

The double-couple nature of earthquakes is well known, as is the resulting pattern of radiated seismic waves [see, e.g., *Sykes*, 1967; *Stauder*, 1968]. The body of literature documenting the effect of radiation pattern on seismic waves with periods of 1–500 s is large. For the periods that typically control peak accelerations of strong motions, 0.1–1.0 s, however, such radiation patterns have not been observed. *Liu and Helmberger* [1985, Figure 14] find that the radiation of an aftershock of the 1979 Imperial Valley earthquake shows a double-couple pattern at a frequency of 1 Hz but not at 2 Hz. These shorter periods, which are of most interest to earthquake engineers, might fail to show a clear radiation pattern for several reasons. Sufficient scattering in the crust, which would affect the short-period energy more than the long-period energy because it has traveled more wavelengths between the earthquake and the seismometers, would tend to blur the radiation pattern into a more uniform distribution. The fault plane itself might not be equally smooth on all scales, and so perhaps short-period seismic radiation is more complex than a double couple. The data in this paper show, however, that at frequencies of 3–6 Hz, the radiation pattern is observable. This result supports the conclusion that these two earthquakes have radiation patterns at high frequencies that are similar to the patterns at longer periods and scattering does not significantly diminish the radiation pattern of the earthquake source.

THE DATA SET OF PEAK ACCELERATIONS

The M_L 5.9 Whittier Narrows earthquake occurred on October 1, 1987. The hypocenter was located at 14.6 km depth, and the mechanism is a gently dipping thrust [*Haukkson and Jones*, this issue]. Numerous aftershocks filled the volume from 8 to 17 km depth extending about 4 km in all directions horizontally. *Bent and Helmberger* [this issue] analyze the teleseismic body waves and propose a double source; their second source is 11 km deep and 5 times larger than the first with a slightly different mechanism. It is important to consider the location and mechanism of the largest patch of moment release to understand the peak accelerations. The double source that they propose is best studied with teleseismic body waves since the strong ground motions are more complicated by the Los Angeles basin near-surface structure. I use the depth and mechanism of their second and largest source to represent the main shock in this paper. The M_L 5.3 aftershock that occurred on October 4, 1987, was located 2 km northwest of the main shock at a depth of 13.3 km, with a strike-slip mechanism on a vertical plane [*Haukkson and Jones*, this issue].

Shakal et al. [1987] collected the data from 22 strong motion stations that recorded both the main shock and the aftershock. *Etheredge and Porcella* [1987, 1988] published records from an additional 30 stations that recorded both events. The locations of these 52 stations are shown in Figure 1. The University of Southern California (USC) also retrieved data for these two earthquakes from about 80 strong motion stations; however, these data are not yet available. Soon, digitized main shock records from the USC network will be available, but the aftershock records are not available in unprocessed form nor is there a schedule for digitizing them. The USC data would fill a large gap in our coverage to the east of the hypocenters, so the conclusions of this paper can be tested against the USC data when it is processed and released. From the USC data, *Trifunac* [1988] has noted that the pattern of peak amplitudes of the main shock differs from the pattern for the aftershock and hypothesizes that this difference is due to the radiation pattern.

The peak horizontal accelerations for both the main shock and the October 4 aftershock for each station are given in Table 1. The peak is estimated by computing the square root of the sum of the squares of the peaks from the published copies of the film records for the two horizontal components. This measure differs from that of *Campbell* [1981], who used the mean of the two horizontal components, and *Joyner and Boore* [1981], who used the larger of the two. The differences between these measures do not affect the conclusions of this paper. A more accurate measure of the peak accelerations would require digitized records and is not yet possible since no aftershock records have yet been digitized. These stations are a mixture of free-field, basement, and ground floor installations. Although basement records have been reported to show smaller peak accelerations than free-field records [*Campbell*, 1981], the difference is small and will not affect the conclusions of this paper, which are drawn only from the ratios of the two events, not the absolute levels.

The peak accelerations from the main shock and the

Paper number 89JB00300.
0148-0227/89/89JB-00300$05.00

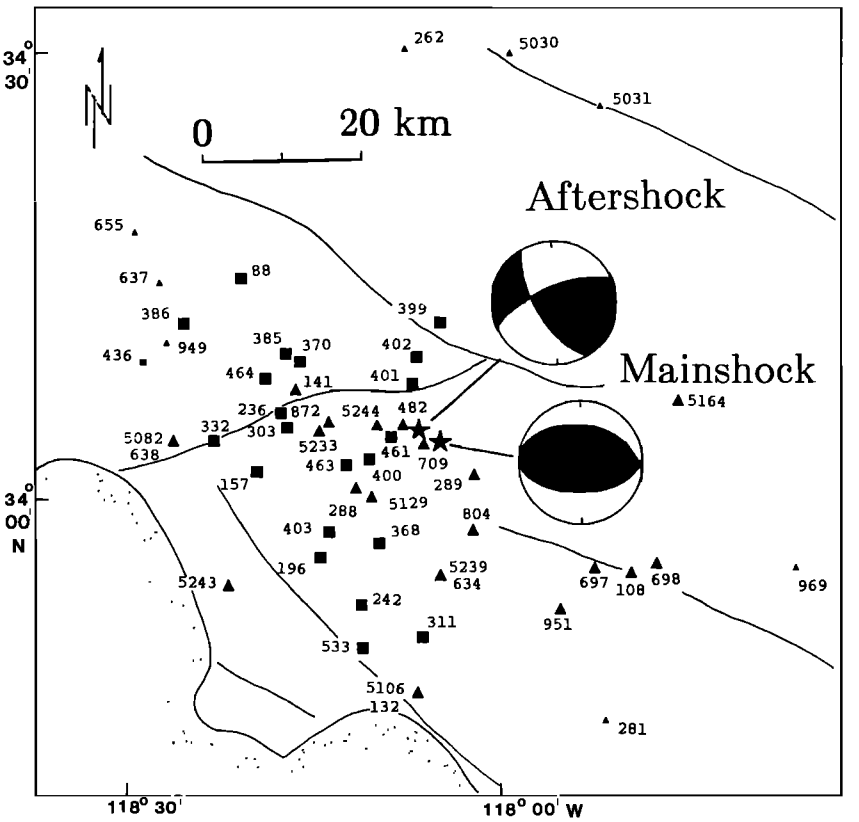

Fig. 1. Map showing the locations of the 52 stations listed in Table 1 that recorded both the October 1 main shock and the October 4 aftershock. Triangles indicate stations described by *Shakal et al.* [1987], and squares indicate stations described by *Etheredge and Porcella* [1987, 1988]. The epicenters given the USGS for the main shock and aftershock are shown as stars. The mechanism for the mainshock is taken from *Bent and Helmberger* [this issue] and the mechanism for the aftershock is taken from *Haukkson and Jones* [this issue]. The light lines show faults and the coastline; see *Haukkson and Jones* [this issue] for a discussion of the regional tectonics.

aftershock are plotted in Figures 2 and 3. The waveforms are all displayed by *Etheredge and Porcella* [1987, 1988] and *Shakal et al.* [1987]. Large changes in peak amplitude occur over short distances. Such changes are not likely to result from radiation pattern, which varies smoothly over the focal sphere, but instead may be the variations in near-receiver focusing, reverberations, and receiver shear impedance that has been amply documented [see, e.g., *Vidale and Helmberger*, 1988]. These near-receiver effects should be minimized by the use of ratios.

Since the main shock and the aftershock have different focal mechanisms and occur in nearly the same place, as seen in Figure 1, the near-receiver effects may be mostly canceled by considering only the ratio between the peak accelerations of the two events. The cancellation will not be perfect because the polarization of the seismic waves incident on each station differs between the two events, and the site response can depend on polarization. Cancellation of station effects by taking the ratio of a pair of events has been a standard tool in studying teleseismic body waves and long-period surface waves.

Figure 4 shows the ratio of peak accelerations from the main shock to those of the aftershock. Most of the horizontal peak accelerations have a peak frequency in the range 3–6 Hz, estimated visually. The ratio averages 2, so the main shock produced about twice the peak acceleration in the 3–6 Hz range as the aftershock, although from standard M_L-moment relations [see, e.g., *Chavez and Priestly*, 1985], the main shock produced 4–8 times more moment release than the aftershock.

Not all stations allow the recovery of a reliable estimate for the ratio of the mainshock peak acceleration to that of the aftershock in a consistent frequency range. Stations 141, 262, 289, 436, 634, 969, 5239, 5030, and 5031 are omitted from Figures 4, 6, and 7. Stations 141, 436, 634, and 5239 are dominated by motions whose frequencies are less than 3 Hz for the main shock, but not the aftershock. Apparently, the main shock produced much more than twice the 1–3 Hz energy of the aftershock. Only stations with similar frequency content for both events will be included in subsequent analysis. Band-pass filtering would allow the use of these records, but fewer than a quarter of the records that we use have been digitized. Stations 262, 5030, and 5031 are too weak (less than 0.02 *g*) to measure reliably the peak acceleration for the aftershock. Station 289 is located on the crest of a dam and shows a strong linear polarization in the same direction for both events, suggesting strong polarization-dependent receiver effects. All the stations were judged with uniform criterion for frequency content and sufficient strength. Station 289 was rejected after its disagreement with the predictions from radiation pattern were noted, but its site on the crest of a dam should have excluded it from consideration at the outset, and no other station of such questionable location are included. The reason for omitting station 969 will be given below.

The peak amplitude ratios shown in Figure 4 vary much

TABLE 1. Stations Recording Both Main Shock and Aftershock

Station	Location		Main Shock Peak Acceleration, Gals	Aftershock Peak Acceleration, Gals	Observed Ratio	Predicted Ratio	Reporting Agency
	Latitude N	Longitude W					
088	34.29°	118.37°	230	70	3.2	1.1	SMIP
157	34.01°	118.36°	230	160	1.4	0.5	SMIP
196	33.90°	118.28°	350	180	1.9	1.0	SMIP
236	34.09°	118.34°	130	80	1.6	0.5	SMIP
242	33.84°	118.19°	290	80	3.6	1.4	SMIP
303	34.09°	118.34°	240	100	2.4	0.5	SMIP
311	33.78°	118.11°	140	80	1.7	0.7	SMIP
332	34.06°	118.42°	100	60	1.8	0.7	SMIP
368	33.92°	118.17°	260	80	3.2	1.4	SMIP
370	34.18°	118.31°	270	150	1.8	0.9	SMIP
385	34.19°	118.31°	280	150	1.9	1.0	SMIP
386	34.22°	118.47°	190	60	3.1	1.1	SMIP
399	34.22°	118.06°	220	220	1.0	0.3	SMIP
400	34.04°	118.18°	630	480	1.3	0.5	SMIP
401	34.11°	118.13°	250	280	0.9	0.8	SMIP
402	34.18°	118.10°	360	360	1.0	0.5	SMIP
403	33.93°	118.26°	490	200	2.4	0.7	SMIP
461	34.07°	118.15°	500	280	1.8	1.2	SMIP
463	34.03°	118.22°	190	270	0.7	0.4	SMIP
464	34.14°	118.36°	140	60	2.3	0.9	SMIP
533	33.77°	118.19°	70	30	2.3	1.2	SMIP
709	34.05°	118.11°	570	280	2.0	0.7	USGS
482	34.09°	118.15°	400	190	2.1	1.0	USGS
5244	34.08°	118.19°	400	240	1.7	0.5	USGS
5129	33.99°	118.16°	570	370	1.5	0.7	USGS
804	33.98°	118.04°	750	460	1.6	0.8	USGS
288	34.00°	118.07°	360	310	1.2	0.5	USGS
872	34.07°	118.25°	190	110	1.7	0.3	USGS
5233	34.05°	118.26°	230	130	1.8	0.3	USGS
697	33.93°	117.88°	310	90	3.4	0.8	USGS
951	33.89°	117.93°	370	150	2.5	0.6	USGS
108	33.92°	117.84°	270	70	3.8	1.0	USGS
5164	34.11°	117.78°	120	40	3.0	0.5	USGS
698	33.91°	117.82°	110	40	2.7	1.4	USGS
132	33.78°	118.11°	130	70	1.9	0.8	USGS
5106	33.78°	118.12°	130	80	1.6	0.8	USGS
5243	33.89°	118.38°	80	50	1.6	1.0	USGS
5082	34.05°	118.45°	100	40	2.5	0.7	USGS
638	34.06°	118.46°	60	30	2.5	0.7	USGS
949	34.17°	118.47°	190	60	3.2	1.1	USGS
637	34.25°	118.48°	280	70	4.0	1.4	USGS
281	33.75°	117.87°	100	30	3.3	0.8	USGS
655	34.31°	118.50°	130	40	3.2	1.5	USGS
969	33.89°	117.64°	180	80	2.2	...	USGS
436	34.16°	118.53°	770	120	6.4	...	SMIP
141	34.12°	118.30°	200	60	3.3	...	USGS
634	33.92°	118.07°	310	70	4.4	...	USGS
5239	33.92°	118.07°	250	80	3.1	...	USGS
262	34.58°	118.11°	50	...	...	...	USGS
5031	34.44°	117.85°	60	...	...	...	USGS
5030	34.52°	117.99°	110	...	...	...	USGS
289	34.03°	118.05°	450	330	1.4	...	USGS

more smoothly than the peak amplitudes shown in Figure 2 and 3. Amplitude ratios less than 1.6 cluster in two pockets located just north and west-southwest of the epicentral region. The ratios above 2.0 cluster in three areas to the west-northwest, south, and southeast of the epicentral region. The smoothness of the variations suggests that most of the near-receiver structure has been canceled out.

In a whole space, the radiation pattern of *S* waves, rather than the weaker *P* waves, determines the strength of body waves as a function of direction from the source. The magnitude of the total *S* wave vector is computed by taking the square root of the sum of the squares of the *SH* and *SV* magnitudes [see, e.g., *Aki and Richards*, 1980]. The total *S* wave pattern has six nodal points evenly spaced around the focal sphere and four lobes evenly spaced on the great circle that passes through the pressure and tension axes. Figures 5*a* and 5*b* show the total *S* wave radiation pattern for the main shock and aftershock focal mechanisms, respectively. The nodal points lie in different places on the focal sphere for the two mechanisms. Figure 5*c* shows the ratio of the two patterns, which may be considered as a prediction of the ratio of the *S* wave amplitudes of the main shock to those of the aftershock.

Figure 6 projects the predicted ratio on the surface of the Earth. A small correction to the pattern seen in Figure 5*c* is required since the two events occurred in slightly different

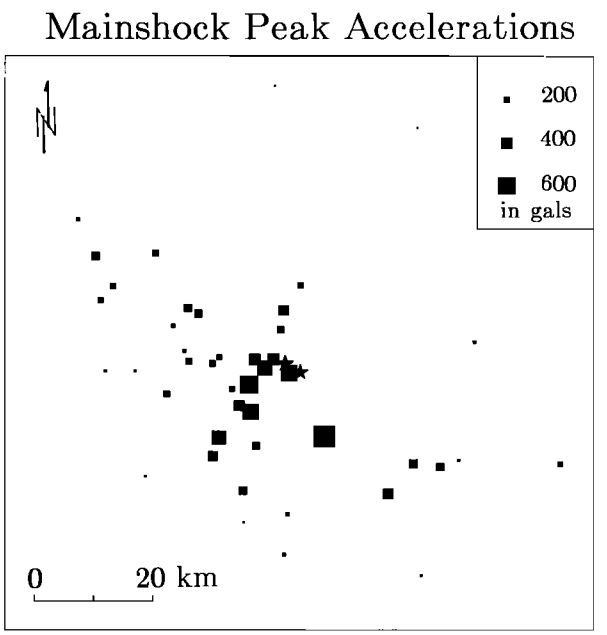

Fig. 2. Map showing the peak horizontal accelerations from the Whittier Narrows main shock for 47 of the stations listed in Table 1. The size of each symbol is proportional to the peak acceleration, which ranges from 50 to 770 Gals.

locations. Thus the rays to nearby receivers depart from the focal sphere at different takeoff angles and azimuths. This projection requires the assumption of a source depth and a velocity structure to convert takeoff angle into epicentral distance. The smooth, laterally invariant basin shear wave velocity structure given in Table 2 is assumed. It is similar to the basin structure given by *Vidale and Helmberger* [1988]. The velocities between the points specified in Table 2 are

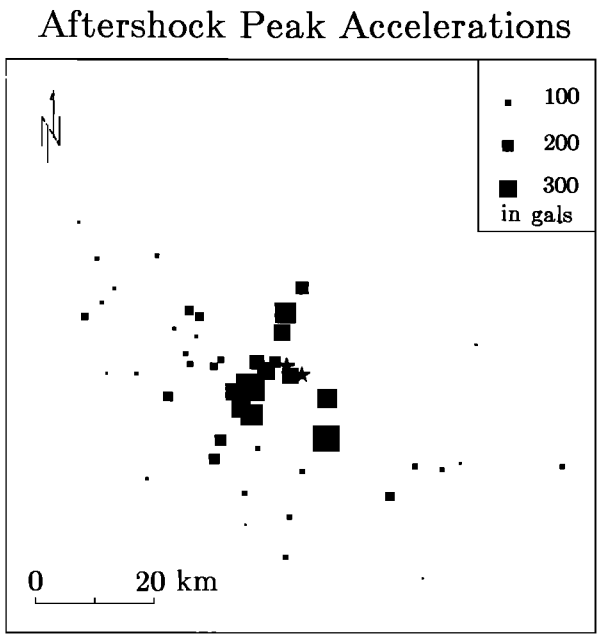

Fig. 3. Map showing the peak horizontal accelerations from the October 4 aftershock for 43 of the stations whose aftershock peak accelerations are listed in Table 1. The size of each symbol is proportional to the peak acceleration, which ranges from 30 to 480 Gals.

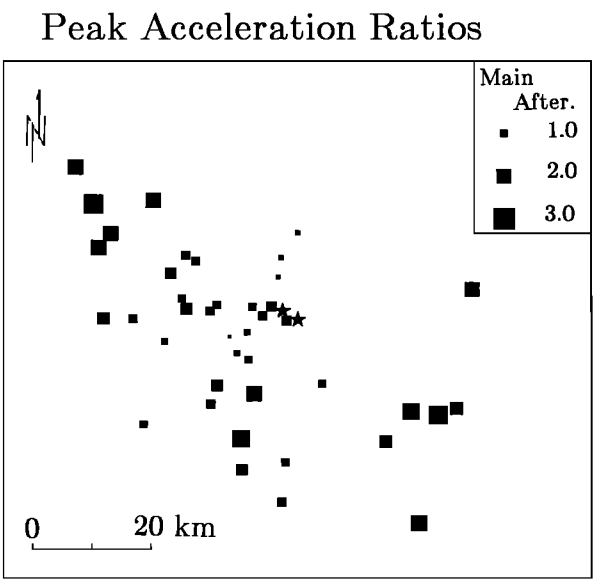

Fig. 4. Map showing peak acceleration from the main shock divided by the peak acceleration from the aftershock for the 43 stations for which a predicted ratio is given in Table 1. The size of each symbol is proportional to the ratio, and the ratios range from 0.7 to 4.0.

linearly interpolated. The range that corresponds to each takeoff angle is determined with the travel time scheme of *Vidale* [1988]. An 11-km depth has been assumed for both sources, following *Bent and Helmberger*'s [this issue] 11-km

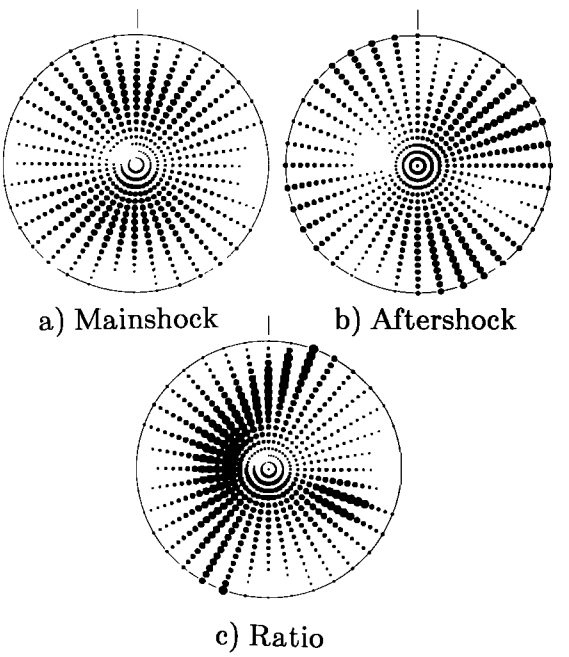

Fig. 5. (*a*) Lower hemisphere projection of the total shear wave radiation pattern for the Whittier Narrows main shock. The symbols are plotted every 10° in azimuth and every 5° in takeoff angle. The size of the symbols is proportional to the strength of the shear waves radiated at that takeoff angle and azimuth. The main shock mechanism was $\phi = 280$, $\delta = 40$, and $\lambda = 98$. (*b*) The shear wave radiation pattern for the Whittier Narrows aftershock. The aftershock mechanism has $\phi = 250$, $\delta = 70$, and $\lambda = 25$. (*c*) The shear wave pattern from the main shock divided by the shear wave pattern of the aftershock. This plot is not corrected for the difference in epicentral location of the two events. The plotting is clipped at a maximum ratio of 2.

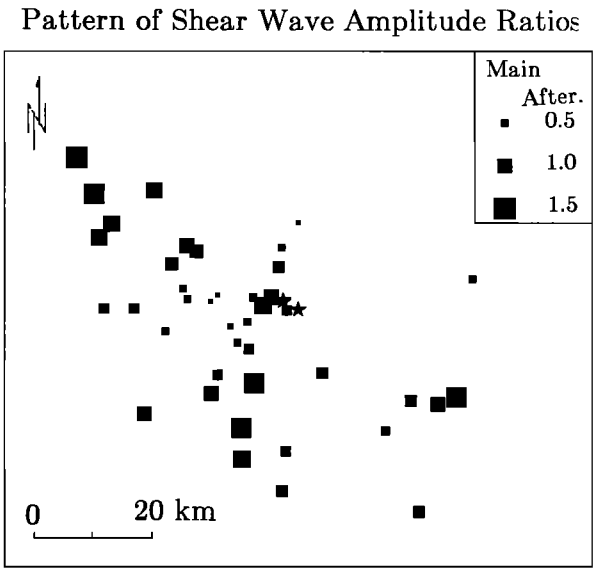

Fig. 6. The ratio of motions from the main shock to motions from the aftershock expected from the S wave mechanism mapped to the Earth's surface. The difference in source location between the main shock and aftershock is taken into account. The size of each symbol is proportionate to the ratio, and the ratios range from 0.3 to 1.5.

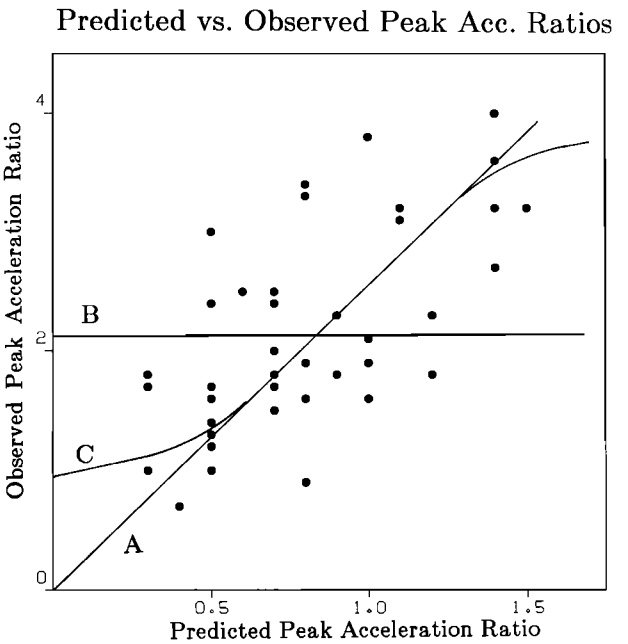

Fig. 7. Predicted ratios of peak accelerations from the main shock and aftershock compared to observed ratios for the first 43 stations listed in Table 1. If the amplitude is proportional to the radiation pattern, the points should scatter around a line that passes through the origin, such as line A. The slope need not be one since the two earthquakes were of different size. If the amplitudes did not depend on focal mechanism, the points would scatter about a horizontal line, such as line B. There is a suggestion that the nodes are not as devoid of seismic energy as predicted, since line C fits marginally better than lines A or B.

depth estimate for the dominant source in the M_L 5.9 main shock and in the absence of any centroid depth estimate for the M_L 5.3 event, for which the aftershocks ranged in depth from 10 to 14 km [*Haukkson and Jones*, this issue]. I do not doubt the deeper epicentral depths, but the 11-km depth that I used probably corresponds to the peak moment release and the source of the peak accelerations. The change in pattern resulting from placing the sources at 14-km depth in accord with their epicentral locations is discussed below.

Comparison between Figures 4 and 6 show that the predicted and observed patterns are very similar. The high and low ratio lobes that appear are all predicted, and all predicted lobes appear, if there are stations located to sample them. The stations nearest the epicenter show a systematic overestimation in the predicted shear wave ratios compared with the observations. Adjusting the locations and the mechanisms of the earthquakes would probably improve the fit. However, I think the results are more unbiased when the initial model is used than if additional free parameters corresponding to variations in mechanisms and locations are introduced after inspecting the misfit. The assumptions of point sources and one-dimensional velocity structure are likely to be the largest sources of errors. If both sources are placed at 14-km rather than 11-km depth, the areas of high and low relative amplitude predicted from the mechanism move farther from the source. Station 969 is not included in Figure 4. The mechanism coefficient for the aftershock is 0.03 and that for the main shock is 0.25, giving a predicted ratio of 8.3, far larger than of the rest of the points in Figure 4. The model predicts that the peak for the main shock would be one fourth of that at a lobe and the peak for the aftershock would be one thirtieth of that at a lobe. The observed ratio of 2.2 indicates that as one might expect, the node for the aftershock is not clean enough to drop the amplitude to only 0.03 of maximum value; therefore this ratio is considered unstable.

TABLE 2. Shear Wave Velocity Model

Depth, km	Velocity, km/s
0	0.6
3	2.0
6	3.6
13	4.2
15	4.4
25	4.4

Figure 7 compares the observed and predicted ratios directly. Despite considerable scatter, a correlation of 0.63 exists between the observed ratio and the ratio of peak accelerations predicted by the focal mechanisms.

DISCUSSION

The influence of focal mechanism on the observed peak acceleration is demonstrated in Figure 7. The ratios of the observed peak accelerations correlate well with the ratios predicted by the focal mechanisms. The scatter seen in Figure 7 may be due to numerous causes. The polarization of the shear waves incident on a station will differ between the two events, and to the extent that the receiver amplification and path effects are functions of polarization, the observations will differ from the predictions. The source locations are assumed to be known, to be small, and to be at the same depth, but the main shock and aftershock are not point sources compared to the shear wavelength at 3–6 Hz, directivity has been shown to affect accelerations [*Boatwright and Boore*, 1982], and the depth of the source of the peak accelerations is not precisely known. Scatter also

arises from variation in the dominant frequency of the peak acceleration. Since the source spectra of the main shock and the aftershock probably differ, the variation in frequency will cause deviations from the predicted pattern. Above, I discarded the four worst cases where the main shock peak accelerations have frequencies markedly lower than the aftershock peak accelerations, but such frequency differences probably remain to some extent.

If the peak acceleration is modulated by the focal mechanism, that is, nodes show very small accelerations, the points in Figure 7 should cluster about a straight line through the origin like line A. If the pattern from the focal mechanism were completely obscured, the points would cluster about the horizontal line B. Line A fits much better than line B. The tendency is that at locations where a node in the radiation pattern is expected, the observed peak acceleration is less and conversely, in a lobe, the peak acceleration is higher.

Line C, with a nonzero intercept but nearly constant slope where the predictions range from 0.5 to 1.5, is the shape of curve I would expect to observe. The nonzero intercept would reflect that some energy is observed where shear wave nodes are predicted, either from scattering of body waves by the geological structures over a solid angle wide enough to partially fill in the nodes or surface waves or *P* waves may fill in where *S* body waves are weak. Small-scale variation in the orientation of the fault plane or slip direction would also tend to obscure the nodes. The data do not require a significantly nonzero intercept.

The strength of the correlation means that these node-filling mechanisms are weak. The correlation between *S* wave strength and peak accelerations means that surface waves are either generated near the receiver or do not influence peak accelerations. In the longer-period range 1–10 s, *Vidale and Helmberger* [1988] show that each basin generates new surface waves, so conversion of shear body waves to surface waves is probably common.

The *S* body waves are not scattered enough to obscure the nodes. Previous studies have not had the advantage of two events with different focal mechanisms in the same place consequently have failed to resolve the radiation pattern at the frequencies of the peak accelerations where receiver effects are also strong. *Boatwright and Boore* [1982] compare two events with a similar focal mechanism, which minimizes differences in motions due to distinct mechanisms, leaving differences that they attributed to directivity. *Liu and Helmberger* [1985] looked for the four-lobed *SH* radiation pattern from an impulsive strike-slip event on the transverse component. They fail to see the pattern at the 4–6 Hz frequency characteristic of the peak accelerations, but they see the pattern emerge when the records are low-passed at 1 Hz. My observations here may disagree with those of *Liu and Helmberger* [1985] for several reasons. Two events with different mechanisms are compared here, while *Liu and Helmberger* [1985] attempted to see the radiation pattern from a single event. The observation of *Liu and Helmberger* [1985] is from the Imperial Valley, which shows extended coda duration, implying that the basin sediments produce more scattering and surface wave generation than most areas. Finally, total *S* strength is used here, allowing *SH* and *SV* mixing, whereas *Liu and Helmberger* [1985] assume no contamination of the transverse component by *SV* energy.

Since the radiation pattern has a measurable effect on the peak accelerations in this case, I address briefly the question of generic patterns that arise from strike-slip and thrust mechanisms. *Joyner and Boore* [1981] and *Campbell* [1981] empirically determined the attenuation of peak acceleration with distance, such empirical formulae could be improved by incorporating focal mechanisms. *Campbell* [1981] examined peak accelerations statistically and notes that reverse faults generate 28% stronger peak accelerations than strike-slip events. A possible explanation of this is obtained by considering that the total shear wave radiation pattern has six nodal points that are located at the pressure, tension, and the neutral axes of the focal sphere. There are also four lobes that are placed along the great circle connecting the pressure and tension axes, each placed midway between a pressure and a tension axis. By considering the *S* wave radiation patterns in Figures 5*a* and 5*b*, for sources placed at 10-km depth in the basin structure described in Table 2, the thrust case is seen to have four nodes for rays that leave the source horizontally, which surface at a distance of 15 km. The two lobes in the lower hemisphere contain rays that surface hundreds of kilometers from the source, outside the regions of strong motions. The two lobes in the upper hemisphere send rays that appear within 10 km of the epicenter.

The strike-slip event also has four nodes for rays that leave the source almost horizontally. The lobes, however, are located such that they concentrate strong motions in the distance range 10–40 km. Depending on the range over which that strong motions are recorded, the thrust pattern could appear to be two patches of very strong shaking surrounded by an area of lesser shaking. The strike-slip case would show a more even distribution of strong and weak shaking. Within 10 km, the thrust event would produce stronger shaking. In the range 10–40 km, the strike-slip event would produce stronger shaking. A similar conclusion may be drawn from the average body wave radiation coefficients listed in Table 5 of *Boore and Boatwright* [1984].

CONCLUSIONS

The focal mechanism modulates the level of peak accelerations in the 1987 Whittier Narrows earthquake and its October 4, 1987, aftershock. This observation precludes great variations in mechanism in the 3–6 Hz range, which corresponds to a 300–1000 m scale length on the fault plane. This also suggests that the energy contributing to the peaks in acceleration left the source region as direct *S* body waves. Scattering does not obscure the influence of earthquake focal mechanism at 3–6 Hz.

Acknowledgments. Support for this work has been provided in part by a grant from the W.M. Keck Foundation and the Institute of Tectonics, University of California, Santa Cruz. The contents of this paper were developed under contract OSMS 8-8068 from the California Department of Conservation, Division of Mines and Geology, Strong Motion Instrumentation Program. However, those contents do not necessarily represent the policy of that agency, and you should not assume endorsement by the state government. Discussion with Donald Helmberger, Antony Shakal, David Boore, and William Savage helped solidify the conclusions. Reviews by Susan Schwartz, Jan Martin, William Joyner, Ross Stein, and an anonymous reviewer clarified the text. A particularly thorough review by Heidi Houston is greatly appreciated. Contribution 54 from the Charles F. Richter Seismological Laboratory at the University of California, Santa Cruz.

REFERENCES

Aki, K., and P. G. Richards, *Quantitative Seismology*, 932 pp., W. H. Freeman, New York, 1980.

Bent, A. L., and D. V. Helmberger, Source complexity of the October 1, 1987, Whittier Narrows earthquake, *J. Geophys. Res.*, this issue.

Boatwright, J., and D. M. Boore, Analysis of the ground accelerations radiated by the 1980 Livermore Valley Earthquake for directivity and dynamic source characteristics, *Bull. Seismol. Soc. Am., 72*, 1843–1865, 1982.

Boore, D. M., and J. Boatwright, Average body-wave radiation coefficients, *Bull. Seismol. Soc. Am., 74*, 1615–1621, 1984.

Campbell, K. W., Near-source attenuation of peak horizontal acceleration, *Bull. Seismol. Soc. Am., 71*, 2039–2070, 1981.

Chavez, D. E., and K. F. Priestly, M_L observations in the Great Basin and M_0 versus M_L relationships for the 1980 Mammoth Lakes, California, earthquake sequence, *Bull. Seismol. Soc. Am., 75*, 1583–1598, 1985.

Etheredge, E., and R. Porcella, Strong-motion data from the October 1, 1987 Whittier Narrows earthquake, *U.S. Geol. Surv. Open File Rep.*, 87–616, 1987.

Etheredge, E., and R. Porcella, Strong-motion data from the Whittier Narrows aftershock of October 4, 1987, *U.S. Geol. Surv. Open File Rep., 88-38*, 1988.

Haukkson, E., and L. Jones, The 1987 Whittier Narrows earthquake sequence in Los Angeles, southern California: Seismological and tectonic analysis, *J. Geophys. Res.*, this issue.

Joyner, W. B., and D. M. Boore, Peak horizontal acceleration and velocity from strong motion records including records from the 1979 Imperial Valley, California, earthquake, *Bull. Seismol. Soc. Am., 71*, 2011–2038, 1981.

Liu, H. L., and D. V. Helmberger, The 23:19 aftershock of the 15 October 1979 Imperial Valley Earthquake: More evidence for an asperity, *Bull. Seismol. Soc. Am., 75*, 689–709, 1985.

Shakal, A. F., M. J. Huang, C. E. Ventura, D. L. Parke, T. Q. Cao, R. W. Sherburne, and R. Blazquez, CSMIP strong-motion records from the Whittier, California earthquake of October 1, 1987, *Rep. OSMS 87-05*, Calif. Strong Motion Instrum. Program, Sacramento, 1987.

Stauder, W., Mechanism of the Rat Island earthquake sequence of February 4, 1965, with relation to island arcs and sea-floor spreading, *J. Geophys. Res., 73*, 3847–3858, 1968.

Sykes, L. R., Mechanism of earthquakes and the mechanics of faulting on the mid-ocean ridges, *J. Geophys. Res., 72*, 2131–2153, 1967.

Trifunac, M. D., The Whittier Narrows, California earthquake of October 1, 1987—Note on peak accelerations during the 1 and 4 October earthquakes, *Spectra, 4*, 101–113, 1988.

Vidale, J. E., Finite-difference travel time calculation, *Bull. Seismol. Soc. Am., 78*, 2062–2076, 1988.

Vidale, J. E., and D. H. Helmberger, Elastic finite-difference modeling of the 1971 San Fernando, Ca. earthquake, *Bull. Seismol. Soc. Am., 78*, 122–142, 1988.

J. E. Vidale, C. F. Richter Seismological Laboratory, Earth Science Board, University of California, Santa Cruz, CA 95064.

(Received October 12, 1988;
revised January 27, 1989;
accepted February 5, 1989.)